NANO LETTERS

Letter

pubs.acs.org/NanoLett

Helium Nanobubbles Enhance Superelasticity and Retard Shear Localization in Small-Volume Shape Memory Alloy

Wei-Zhong Han,*[,†] Jian Zhang,[‡] Ming-Shuai Ding,[†] Lan Lv,[†] Wen-Hong Wang,[§] Guang-Heng Wu,[§] Zhi-Wei Shan,*[,†] and Ju Li*[,†,∥]

[†]Center for Advancing Materials Performance from the Nanoscale and Hysitron Applied Research Center in China, State Key Laboratory for Mechanical Behavior of Materials, Xi'an Jiaotong University, Xi'an 710049, People's Republic of China

[‡]College of Energy, Xiamen University, Xiamen 361005, People's Republic of China

[§]Beijing National Laboratory for Condensed Matter Physics, Institute of Physics, Chinese Academy of Sciences, Beijing, 100190, People's Republic of China

[∥]Department of Nuclear Science and Engineering and Department of Materials Science and Engineering, Massachusetts Institute of Technology, Cambridge, Massachusetts 02139, United States

Supporting Information

ABSTRACT: The intriguing phenomenon of metal superelasticity relies on stress-induced martensitic transformation (SIMT), which is well-known to be governed by developing cooperative strain accommodation at multiple length scales. It is therefore scientifically interesting to see what happens when this natural length scale hierarchy is disrupted. One method is producing pillars that confine the sample volume to micrometer length scale. Here we apply yet another intervention, helium nanobubbles injection, which produces porosity on the order of several nanometers. While the pillar confinement suppresses superelasticity, we found the dispersion of 5−10 nm helium nanobubbles do the opposite of promoting superelasticity in a $Ni_{53.5}Fe_{19.5}Ga_{27}$ shape memory alloy. The role of helium nanobubbles in modulating the competition between ordinary dislocation slip plasticity and SIMT is discussed.

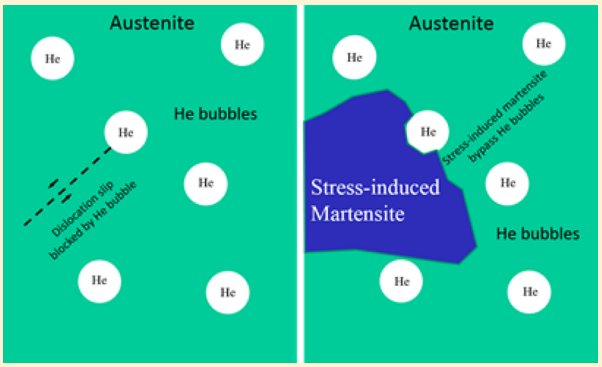

KEYWORDS: *Shape memory alloy, irradiation, phase transformation, superelasticity, helium bubble*

Small-volume smart materials with dimension on the order of micrometer are used in MEMS, NEMS, and other devices. The component length scale D can strongly interfere with the intrinsic length scales in smart materials, for example, those of hierarchical space-filling martensites, thus affecting their basic function. Shape memory alloy (SMA) is a class of smart materials often used in microactuators that demonstrates the shape memory and superelasticity effects through reversible transformations between a high-temperature austenite phase and a low-temperature martensite phase.[1] The SMA performance at micro- or submicroscales have attracted broad attention[2−4] because of applications in devices such as microfluidic valves and pumps, electromechanical switches, and so forth.

Several studies have indicated that the superelastic response of SMA pillars has a strong size-dependence.[5−14] Ozdemir et al.[13] reported that the superelasticity of [110] $Ni_{54}Fe_{19}Ga_{27}$ shape memory alloy single crystal pillars start to diminish once the diameter of pillars $D < \sim 1$ μm. It was suggested that the irreversible plastic deformation observed is due to the formation of stabilized martensites, even though there was no direct experimental evidence. Certainly, ordinary dislocation slip plasticity (ODP) could also contribute to plastic strain.[15−19] ODP also has a size dependence,[15−19] thus it is crucial to understand the size-dependent mechanisms of irreversible plasticity veresus reversible superelasticity of SMA, so we can utilize superelasticity above a critical component size D_{min} (superelasticity).

Helium ion (α) irradiation is an effective way to introduce an additional length scale control parameter into the problem.[20−22] Helium is a noble gas and does not chemically react or mix with solid elements, so when it is injected into an alloy, gas bubbles will form inside.[20−22] The range of the implanted helium depends on the energy, but it is generally on the order of few hundred nanometers to micrometers, thus matching well with the aforementioned component length scale of small-volume devices. Furthermore, present ion beam technology allows the helium-beam to be localized to nanometers, thus enabling in-plane patterning. For these reasons, in this study we will use helium nanobubbles

Received: March 9, 2017
Revised: May 3, 2017
Published: May 10, 2017

DOI: 10.1021/acs.nanolett.7b01015
Nano Lett. 2017, 17, 3725−3730

introduced by α-radiation to modulate the size-dependent competition between dislocation-based ODP and phase transformation based superelasticity in a model SMA.

Here we choose Ni−Fe−Ga shape memory alloy, which shows large superelastic recoverable strains (12−13%) and stable cyclic superelasticity in bulk,[23−27] as a model material to explore the size-dependent ODP versus superelasticity. $Ni_{53.5}Fe_{19.5}Ga_{27}$ single crystal with [001] orientation was used[28] and was compressed uniaxially in situ. Differential scanning calorimetry was employed to measure the characteristic phase transformation temperatures (see Figure S1), and we obtained M_s = 276 K, M_f = 269 K, A_s = 275 K, and A_f = 283 K. Thus, the starting phase for our Ni−Fe−Ga at room temperature is austenite ($L2_1$) and is suitable for probing the superelasticity under mechanical loading. The crystallographic orientations were determined by Laue diffraction and electron backscatter diffraction before sample cutting. Following the standard procedures,[21,22] micron-sized and submicron-sized pillars with [001] orientation were fabricated via FIB micromachining. The single crystal Ni−Fe−Ga pillars have a typical height to diameter ratio of 3:1. During the FIB processing, we have taken precaution to minimize the FIB-related damages.[21,22] In situ compression tests were conducted using a Hysitron PicoIndenter (PI87) inside a scanning electron microscope (SEM) at room temperature (~293 K). The compression strain rate was set to be $\sim 10^{-3}$/s for all tests. For some deformed pillars, FIB-lift out technique was used to prepare thin foils and then the deformed microstructures were characterized by transmission electron microscopy (TEM). Helium implantation was performed on [001] Ni−Fe−Ga single crystal to a fluence of 2×10^{17} ions/cm^2 by using 400 keV helium ions at 200 °C. Then in situ compression tests were performed on the Ni−Fe−Ga pillars containing high density of helium bubbles. More than 30 compression tests were performed successfully on [001] Ni−Fe−Ga pillars with and without helium implantation. All the tests were recorded with a charge coupled device camera.

Figure 1 displays the typical compressive stress−strain curves of a [001] Ni−Fe−Ga pillar with initial sample diameter of D = 2.35 μm. The pillar shows obvious superelasticty with a martensitic transformation stress σ_c = 700 MPa, which is much higher than the bulk [001] Ni−Fe−Ga single crystal (σ_c = 103 MPa),[29] showing a strong size-dependent superelasticity in agreement with previous studies.[5,12] Significant stress−strain hysteresis was seen during unloading from the maximum compressive strain of ~2.75%, as shown in Figure 1. After removing the flat indenter, the pillar comes back to the original height, showing the typical character of superelasticity (Figure 1). The pillar morphology before and after loading are displayed as insets in Figure 1. During compression, the diameter of Ni−Fe−Ga pillar has widened obviously, but the pillar diameter returned to the original size after removing the loading.

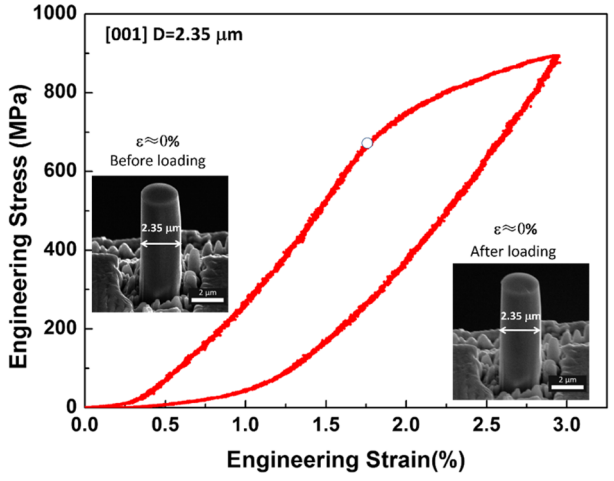

Figure 1. Compressive stress−strain curves of [001] Ni−Fe−Ga single crystal pillar with diameter of 2.35 μm. The fully recovered compression strain upon unloading is the typical feature of superelasticity induced by austenite to martensite phase transformation. The inset images showing the shape evolution of the [001] Ni−Fe−Ga pillar before and after loading.

As D of the single crystal pillar further reduces, a transition from superelasticity to permanent plastic deformation was evidenced. Figure 2 shows a typical example of compressive loading of [001] Ni−Fe−Ga pillar with initial diameter of 890 nm. At the initial loading stage, the stress−strain curve shows a nearly linear relationship, indicating purely elastic deformation, identical to the behavior of the larger pillar in Figure 1. When the compressive stress reaches ~700 MPa, a small strain burst appears, which likely corresponds to some localized ODP but it is not obvious based on the in situ video (Movie S1), then the stress continuously increases following the original trend with further loading in contrast to stress−strain curve in Figure 1, that suggests no obvious SIMT is happening at this stage. Further elevating the compressive stress to ~900 MPa, a second strain burst takes place, corresponding to the nucleation of a small shear band (white line) on the pillar, as marked in the inset in Figure 2, and as a result the compressive stress decreases slightly. We denote this point as the ODP yield point. With the test proceeding, the compressive stress keeps increasing linearly, and at ~1250 MPa a big strain burst occurs, following the formation of a fresh new major shear band across the pillar, as shown in Movie S1 and labeled on the inset in Figure 2. After unloading, all the shear bands remain on the pillar with big surface steps, resulting in ~8% permanent plastic

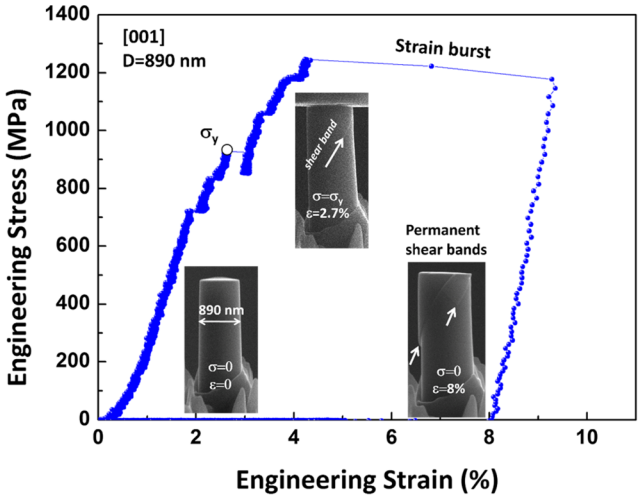

Figure 2. Compressive stress−strain curves of a [001] Ni−Fe−Ga single crystal pillar with diameter of 890 nm. The big strain burst occurs during mechanical loading indicating the plastic deformation of Ni−Fe−Ga single crystal pillar. The inset SEM images show the shear deformation features formed on [001] Ni−Fe−Ga pillar during compression.

DOI: 10.1021/acs.nanolett.7b01015
Nano Lett. 2017, 17, 3725−3730

deformation, as shown in Figure 2. Ozdemir et al.[13] reported that the [110] Ni−Fe−Ga pillars also start to show irreversible deformation for pillar with diameter around 500 nm. All of these experimental results support that the superelasticity of Ni−Fe−Ga shape memory alloy pillars have a strong size-dependence (e.g., as reflected in the activation stress[12]), and superelasticity will disappear once a lower limit of pillar diameter D_{min}(superelasticity) is reached.

Figure 3 summarizes the variation of martensitic phase transformation stress and the yielding stress of [001] Ni−Fe−Ga pillars with D. We used open symbols for these pillars showing clear superelasticity, while marked as solid symbols for the pillars demonstrating permanent deformation. There is a clear transition from superelasticity to plastic deformation for [001] Ni−Fe−Ga single crystal pillars at D_{min}(superelasticity) ≈ 1.2 μm. Several researchers suggested that the loss of superelasticity in shape memory alloy pillars is due to the formation of stabilized martensites but this lacks direct experimental evidence.[12,13] In our study, we have examined the permanently deformed pillars. As displayed in Figure S2, a [001] Ni−Fe−Ga pillar with diameter of ∼900 nm was loaded to produce a major shear band (as marked), then the test was stopped and a TEM thin foil was cut from the middle of the deformed pillar for further characterization. Figure S2b is the typical TEM image taken from this region, showing two inclined white bands corresponding to the shear bands formed during compression. A selected area diffraction pattern was taken on the region marked by the dash line cycle, as insert in Figure S2b. This diffraction pattern is the typical austenite [110] diffraction of the Ni−Fe−Ga single crystals, showing the plastic deformation in these pillars are resulting from the ODP/shear localization rather than the nucleation of stabilized martensites as suggested previously.[13] More selected area diffraction analyses were performed across the whole pillar and only austenite phase was detected. These results demonstrated that a transition from superelasticity to ODP occurs when the pillar diameter is less than D_{min}(superelasticity) ≈ 1.2 μm. Interestingly, a mechanism switch from deformation twinning to ODP was also observed in a family of Ti alloy pillars at D ∼ 1 μm.[15]

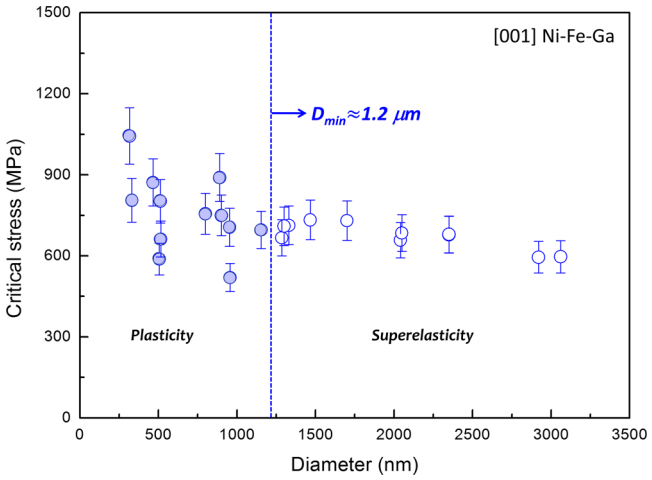

Figure 3. Variation of critical stress for SIMT and ODP of [001] Ni−Fe−Ga single crystal pillars with diameters. A transition from superelasticity to plasticity occurs at pillar diameter of ∼1.2 μm. Open symbols for pillars show superelasticity, solid symbols for pillars display plasticity.

To retard the tendency of shear localization of submicron-sized Ni−Fe−Ga pillars, we implant nanoscale helium bubbles before the compression test. Helium nanobubbles have been shown to be effective in stabilizing the ODP of small-volume metallic pillars.[22] In addition, it has been proposed that porous structures benefit the shape memory effect via release of the space-filling constraint effect on phase transformation, although this has only been tested at much larger pore sizes.[30,31] Figure 4a shows the distribution of radiation damage in displacements per atom (dpa) and helium concentration in Ni−Fe−Ga after ion accelerator-based helium implantation. The peak helium concentration appears at around the depth of ∼1.2 μm from the top surface of implantation and the high bubble density region has a width of ∼500 nm, as marked in Figure 4a. The high density of helium bubbles structures are highlighted in Figure 4b. These helium bubbles have a typical size in the range of 5 to 10 nm, and some of them display faceted feature. According to the selected area diffraction pattern in Figure 4b, the Ni−Fe−Ga still largely remained in the austenite phase ($L2_1$) after a high dose of helium implantation,[32] thus these helium nanobubbles mainly affect Ni−Fe−Ga through an internal length scale effect at the very fine length scale end of nanodispersions like in oxide-dispersion strengthened alloys (ODS).[33]

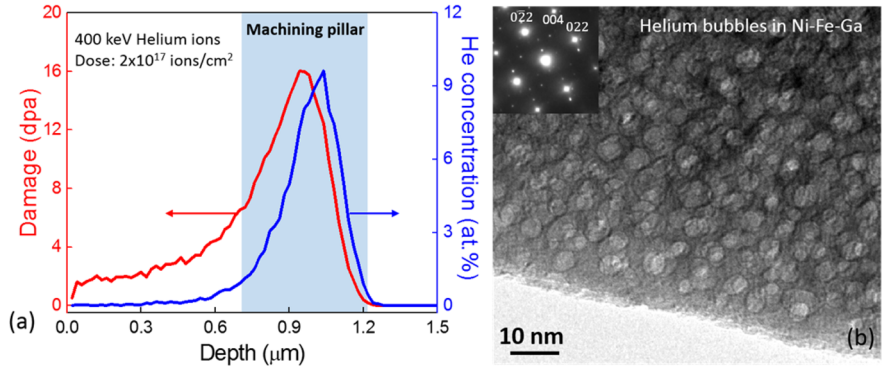

Figure 4. (a) The variation of radiation damage and helium concentration in [001] Ni−Fe−Ga single crystal after helium implantation. The peak helium concentration appears in the region around 1 μm distance from the implanting surface. (b) Typical TEM image of helium bubbles formed in [001] Ni−Fe−Ga single crystal after helium implantation. The inset selected area electron diffraction pattern indicates the helium bubbles implanted Ni−Fe−Ga still remained largely as austenite phase with $L2_1$ crystal structure with long-range order (indicated by the weak diffraction spots).

DOI: 10.1021/acs.nanolett.7b01015
Nano Lett. 2017, 17, 3725−3730

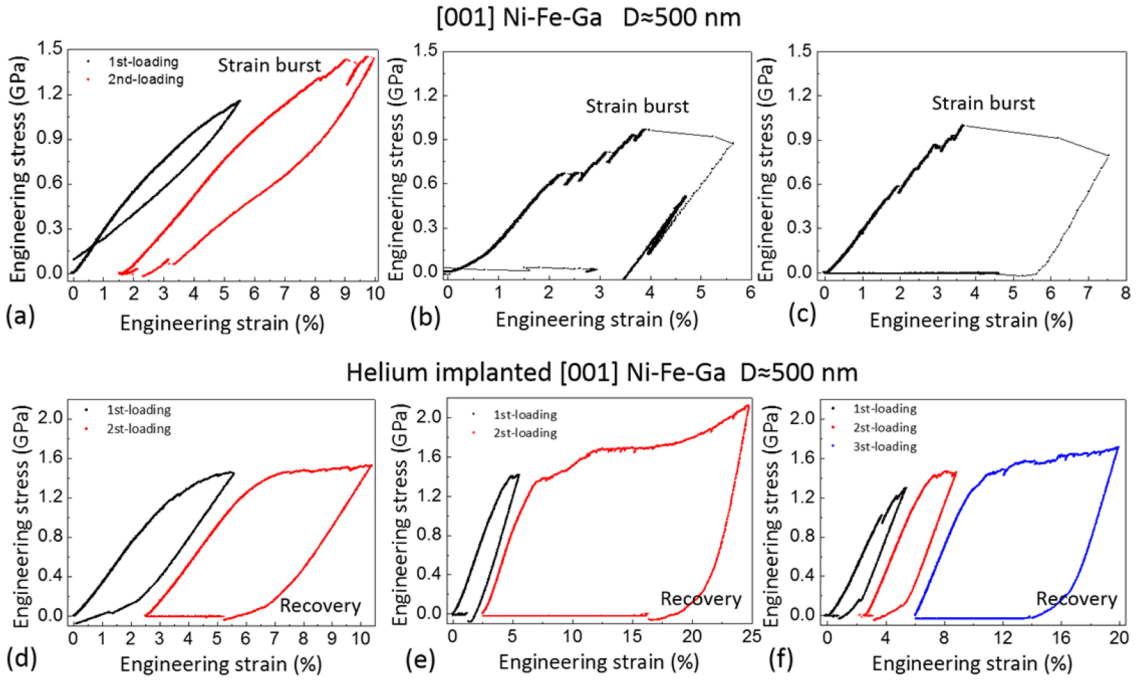

Figure 5. (a–c) The compressive behavior of [001] Ni–Fe–Ga single crystal pillars with diameter of 500 nm. (d–f) The compressive behavior of helium bubbled [001] Ni–Fe–Ga single crystal pillars with diameter of 500 nm. High density of helium bubbles lead to a stable stress strain response of Ni–Fe–Ga pillar, a lower critical stress for inverse phase transformation and 2% of recoverable strain after unloading.

Within the high helium concentration regions, we used FIB to machine [001] oriented Ni–Fe–Ga pillars with the typical diameter of 500 nm across the high bubble density region, as marked in Figure 4a. In contrast to Figure 3, which showed formation of shear band and loss of superelasticity, in Figure 5 the Ni–Fe–Ga pillars containing high density of helium bubbles show improved superelasticity. To facilitate comparison, we machined six pillars with diameter of 500 nm. The first group of three pillars are helium free, and the second group of three pillars contain high density of helium nanobubbles. We then performed compression test on these D = 500 nm pillars using the method introduced above. As shown in Figure 5a, two out of three of the helium-free Ni–Fe–Ga pillars show the obvious permanent plastic deformation, such as big strain burst and shear bands formation, as displayed in Figure 5b,c and Figure S3a. The first pillar shows some tendency of superelasticity at small strain but small strain bursts frequently appeared with the increase of the strain, as indicated in Figure 5a. In contrast, the Ni–Fe–Ga pillars containing high density of helium bubbles show full or partial superelasticity at different applied strains, as displayed in Figure 5d–f. At the applied strain of 3%, two out of three Ni–Fe–Ga pillars show full superelasticty at the diameter of 500 nm, such as the cases shown in Figure 5d,f. With further increasing the applied strain to larger than 5%, the stress–strain response of helium bubbled pillars are very stable, almost no any significant strain bursts take place, as shown in Figure 5d–f. The critical stress of helium implanted pillars is ~1.2 GPa or even higher, which is roughly 2-fold of the critical stress for helium free pillars (0.6–0.8 GPa), indicating the significant strengthening after helium implantation. During the unloading, all the three pillars with internal helium nanobubbles show 2% recoverable strain and a low critical stress (~0.3 GPa) for the inverse phase transformation, as marked in Figure 5d–f. After unloading, the deformed pillars were characterized by the scanning electron microscopy and all of the pillars containing helium nanobubbles do not show any shear banding surface relief; a typical example is shown in Figure S3b, which is in contrast to the shear localized deformation of helium-free pillars (Figure 2 and Figure S3a). Our current studies indicated that the implantation of helium nanobubbles can improve the superelasticity and retard the tendency of shear localization by ODP in submicron-sized Ni–Fe–Ga pillars. This results in much more predictable deformation path and improves the "mechanical controllability index" of small-volume materials.[34]

The above observations indicate that the austenite phase is stabilized in these submicron-sized pillars and a transition from superelasticity to plasticity occur once the pillar diameter less than D_{min}(superelasticity) ≈ 1.2 μm in Ni–Fe–Ga. Because of the geometrical constraint effect of submicron-sized pillars, the difficulty of the nucleation of martensites is likely a reason leading to the size-dependent superelasticity. In general, the nucleation sites for martensites are usually located at grain boundaries, dislocations, or any stress-concentrating defects.[12,35,36] But in small-volume single crystal pillars, there is a quick reduction of internal defects density with narrowing-down of the pillar diameter.[12,21] For these reasons, higher stresses are needed to activate martensitic phase transformation, thus leading to the increase in martensitic transformation stress of small-volume shape memory alloy pillars (Figure 1).[12,13] With further reduction of the pillar diameter, once the required stress for martensites nucleation is larger than the yielding stress of austenite, the pillar starts to deform plastically rather than triggering martensitic phase transformation (Figure 2). The microstructural characterization shown in Figure S2 indicates that there are no martensites nucleation in the plastically deformed pillars, and this finding also supports the martensitic phase transformation difficulty hypothesis.

DOI: 10.1021/acs.nanolett.7b01015
Nano Lett. 2017, 17, 3725–3730

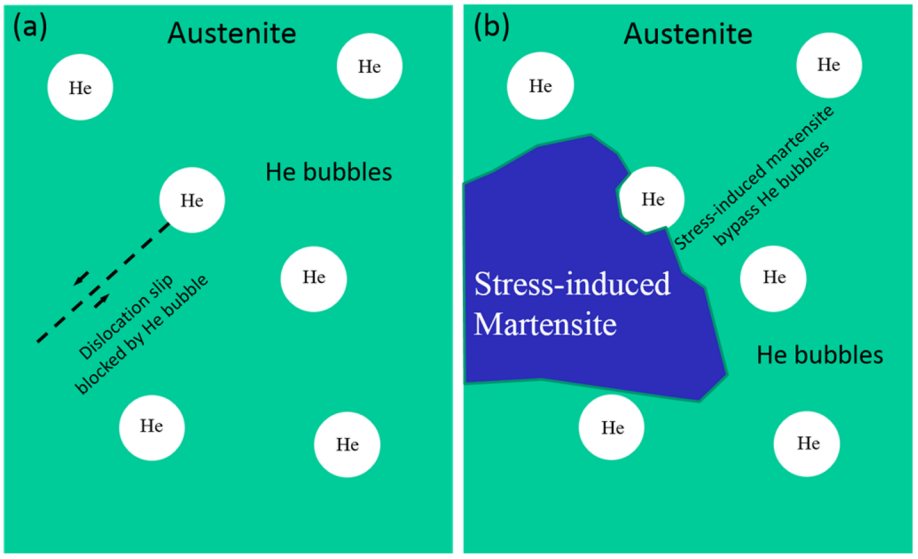

Figure 6. Schematic illustration of the dislocation/martensite interaction with helium bubbles in [001] Ni−Fe−Ga single crystal pillars. (a) Localized dislocation slip is easily blocked by helium bubbles due to its narrower width compared to bubble size. (b) Stress-induced martensite is capable of bypassing the nanoscale helium bubbles because their nucleation size is larger than the He bubble.

Because of the above reasons, the implantation of helium nanobubbles could partially relieve the geometrical constraint effect on martensitic phase transformation and retard the shear localization in submicron-sized pillars. During the deformation of Ni−Fe−Ga pillars, the implanted helium bubbles could play a role of martensitic nucleation sites as the other internal defects reported.[12,30,31] The significant increase of the critical stress of helium-implanted pillar is likely due to the profuse martensite−martensite and martensite−bubble interactions, as shown in Figure 5d−f. Furthermore, a large number of helium nanobubbles create large area of internal surface inside a small-volume pillar, which will compensate the surface energy contribution to the total free energy of martensitic phase transformation due to large surface area to volume ratio of martensite in a small-volume pillar[37,38] In addition, the pressurized helium nanobubbles are strong obstacles for dislocation slip,[21,22] as schematically illustrated in Figure 6a, thus it has the ability to block shear localization, promote martensite−martensite and martensite−bubble interactions and thus increase the yield stress; this is why the submicron-sized Ni−Fe−Ga pillars show quite stable plastic deformation once the applied strain are larger than 5%, as shown in Figure 5d−f. In contrast, the nanoscale helium bubbles have less blocking effect on stress-induced martensitic because the martensitic nuclei are larger than the bubble size,[4] hence the martensite could bypass the helium nanobubbles, as illustrated in Figure 6b. Furthermore, the interaction between martensitic with helium nanobubbles will produce a strong back stress, which will assist the reversal phase transformation, as manifested by the low critical stress and the recoverable strain observed in Figure 5d−f. Thus, the implantation of helium nanobubbles is a highly effective method to tune the superelasticty of small-volume SMA. In this study, the submicron-sized Ni−Fe−Ga pillars only show full superelasticty at small strain and partial superelasticty at larger strain, which is likely due to the inhomogeneous distribution of helium nanobubbles across the pillar (high bubble density in the middle and low bubble density near the edge, as shown in Figure 4a). The Ni−Fe−Ga pillars containing homogeneous distribution of helium nanobubbles might have better superelasticity.

In our experiments, Ni−Fe−Ga pillars show strongly size-dependent superelasticity and dislocation plasticity. Once the pillar diameter is less than ∼1.2 μm, martensitic phase transformation will be suppressed and the deformation takes place via irreversible shear localization by ODP. By helium implantation to form numerous internal nanobubbles in Ni−Fe−Ga pillars, the superelasticity of submicron-sized Ni−Fe−Ga pillar could be improved. The helium bubbled pillars have higher martensitic transformation stress and more stable stress−strain response, greatly improving the "mechanical controllability index" of small-volume materials,[34] which is a boon for device applications. The internally pressurized helium nanobubbles likely promote the nucleation of martensitic embryos and assists the reversible phase transformation, and simultaneously reduce the chance of shear localization. These findings open new avenues for tuning the superelasticity of small-volume shape memory alloy via helium nanobubble engineering.

In conclusion, helium bubble implantation is shown to be an effective way to tune an internal length scale effect on superelasticity and plasticity. It clearly changes the superelasticity versus plasticity competition, based on phase transformation and dislocation slip mechanism, respectively, for micron-scale material components. Helium bubbles act on the very fine scale end of nanodispersions, like in oxide-dispersion strengthened steels (ODS). Unlike ODS, helium bubble injection is much more easily tunable (by varying the kinetic energy, flux, and duration of radiation) and is spatially patternable at micron resolution (e.g., "helium bubble printing"), thus facilitating the functional control of small-volume smart materials.

■ ASSOCIATED CONTENT

Supporting Information

The Supporting Information is available free of charge on the ACS Publications website at DOI: 10.1021/acs.nanolett.7b01015.

DOI: 10.1021/acs.nanolett.7b01015
Nano Lett. 2017, 17, 3725−3730

Three supporting figures of the microstructures and deformation features of Ni-Fe-Ga (PDF)
Video of the in situ mechanical tests (AVI)

AUTHOR INFORMATION

Corresponding Authors

*E-mail: wzhanxjtu@mail.xjtu.edu.cn.
*E-mail: zwshan@mail.xjtu.edu.cn.
*E-mail: liju@mit.edu.

ORCID

Wei-Zhong Han: 0000-0001-7982-4042
Ju Li: 0000-0002-7841-8058

Author Contributions

W.Z.H., Z.W.S., and J.L. conceived the idea, W.Z.H. designed the research, W.Z.H. and J.Z. performed the helium implantation, M.S.D. and L.L. conducted the in situ compression test, W.H.W. and G.H.W. prepared the sample, and W.Z.H. and J.L. wrote the paper. All authors contributed to the discussion of the data.

Notes

The authors declare no competing financial interest.

ACKNOWLEDGMENTS

This work was supported by the National Natural Science Foundation of China (Grant Nos. 51471128, 51231005, 51621063, and 51471184). W.Z.H. would like to thank the support of Youth Thousand Talents Program of China, the National Key Research and Development Program of China (SQ2017YFGX090025), and the Young Talent Support Plan of XJTU. J.L. acknowledges support by NSF DMR-1410636.

REFERENCES

(1) Otsuka, K.; Wayman, C.M.. *Shape Memory Materials*; Cambridge University Press, 1998.
(2) Bhattacharya, K.; James, R. D. *Science* **2005**, *307*, 53.
(3) Kohl, M. *Shape Memory Microactuators*; Springer: Berlin, 2004.
(4) Liu, L. F.; Ding, X. D.; Li, J.; Lookman, T.; Sun, J. *Nanoscale* **2014**, *6*, 2067.
(5) San Juan, J.; No, M. L.; Schuh, C. A. *Adv. Mater.* **2008**, *20*, 272.
(6) Chen, Y.; Schuh, C. A. *Acta Mater.* **2011**, *59*, 537.
(7) Lai, A.; Du, D. H.; Gan, C. L.; Schuh, C. A. *Science* **2013**, *341*, 1505.
(8) Frick, C. P.; Orso, S.; Arzt, E. *Acta Mater.* **2007**, *55*, 3845.
(9) Frick, C. P.; Clark, B. G.; Orso, S.; Sonnweber-Ribic, P.; Arzt, E. *Scr. Mater.* **2008**, *59*, 7.
(10) Frick, C. P.; Clark, B. G.; Schneider, A. S.; Maab, R.; Van Petegem, S.; Van Swgenhoven, H. *Scr. Mater.* **2010**, *62*, 492.
(11) Ye, J.; Mishra, R. K.; Pelton, A. R.; Minor, A. M. *Acta Mater.* **2010**, *58*, 490.
(12) San Juan, J.; No, M. L.; Schuh, C. A. *Nat. Nanotechnol.* **2009**, *4*, 415.
(13) Ozdemir, N.; Karaman, I.; Mara, N. A.; Chumlyakov, Y. I.; Karaca, H. E. *Acta Mater.* **2012**, *60*, 5670.
(14) Liu, L. F.; Ding, X. D.; Sun, J.; Li, S. Z.; Salje, E. K. H. *Nano Lett.* **2016**, *16*, 194.
(15) Yu, Q.; Shan, Z. W.; Li, J.; Huang, X. X.; Xiao, L.; Sun, J.; Ma, E. *Nature* **2010**, *463*, 335.
(16) Zheng, K.; Han, X. D.; Wang, L. H.; Zhang, Y. F.; Yue, Y. H.; Qin, Y.; Zhang, X. N.; Zhang, Z. *Nano Lett.* **2009**, *9*, 2471.
(17) Yue, Y. H.; Liu, P.; Zhang, Z.; Han, X. D.; Ma, E. *Nano Lett.* **2011**, *11*, 3151.
(18) Wang, Y. B.; Wang, L. F.; Joyce, H. J.; Gao, Q. A.; Liao, X. Z.; Mai, Y. W.; Tan, H. H.; Zou, J.; Ringer, S. P.; Gao, H. J.; Jagadish, C. *Adv. Mater.* **2011**, *23*, 1356.
(19) Han, W. Z.; Huang, L.; Ogata, S.; Kimizuka, H.; Yang, Z. C.; Weinberger, C.; Li, Q. J.; Liu, B. Y.; Zhang, X. X.; Li, J.; Ma, E.; Shan, Z. W. *Adv. Mater.* **2015**, *27*, 3385.
(20) Liontas, R.; Gu, X. W.; Fu, E. G.; Wang, Y. Q.; Li, N.; Mara, N.; Greer, J. R. *Nano Lett.* **2014**, *14*, 5176.
(21) Ding, M. S.; Du, J. P.; Wan, L.; Ogata, S.; Tian, L.; Ma, E.; Han, W. Z.; Li, J.; Shan, Z. W. *Nano Lett.* **2016**, *16*, 4118.
(22) Ding, M. S.; Tian, L.; Han, W. Z.; Li, J.; Ma, E.; Shan, Z. W. *Phys. Rev. Lett.* **2016**, *117*, 215501.
(23) Oikawa, K.; Ota, T.; Ohmori, T.; Tanaka, Y.; Morito, H.; Fujita, A.; Kainuma, R.; Fukamichi, K.; Ishida, K. *Appl. Phys. Lett.* **2002**, *81*, 5201.
(24) Sutou, Y.; Kamiya, N.; Omori, T.; Kainuma, R.; Ishida, K.; Oikawa, K. *Appl. Phys. Lett.* **2004**, *84*, 1275.
(25) Liu, Z. H.; Wu, G. H.; Liu, Y. *Intermetallics* **2006**, *14*, 1493.
(26) Efstathiou, C.; Sehitoglu, H.; Kurath, P.; Foletti, S.; Davoli, P. *Scr. Mater.* **2007**, *57*, 409.
(27) Efstathiou, C.; Sehitoglu, H.; Carroll, J.; Lambros, J.; Maier, H. J. *Acta Mater.* **2008**, *56*, 3791.
(28) Qian, J. F.; Zhang, H. G.; Chen, J. L.; Wang, W. H.; Wu, G. H. *J. Cryst. Growth* **2014**, *388*, 107.
(29) Liu, Z. H.; Ma, X. Q. *Acta Phys. Sin.* **2012**, *61*, 028103.
(30) Chmielus, M.; Zhang, X. X.; Witherspoon, C.; Dunand, D. C.; Mullner, P. *Nat. Mater.* **2009**, *8*, 863.
(31) Bewerse, C.; Brinson, L. C.; Dunand, D. C. *Acta Mater.* **2016**, *115*, 83.
(32) Satto, C.; Jansen, J.; Lexcellent, C.; Schryvers, D. *Solid State Commun.* **2000**, *116*, 273.
(33) Klueh, R. L.; Shingledecker, J. P.; Swindeman, R. W.; Hoelzer, D. T. *J. Nucl. Mater.* **2005**, *341*, 103.
(34) Wang, Z. J.; Shan, Z. W.; Li, J.; Sun, J.; Ma, E. *Sci. China: Technol. Sci.* **2014**, *57*, 663.
(35) Shaw, J. A.; Kyriakides, S. *Acta Mater.* **1997**, *45*, 683.
(36) Waitz, T.; Kazykhanov, V.; Karnthaler, H. P. *Acta Mater.* **2004**, *52*, 137.
(37) Li, S. Z.; Ding, X. D.; Li, J.; Ren, X. B.; Sun, J.; Ma, E. *Nano Lett.* **2010**, *10*, 1774.
(38) Li, S. Z.; Ding, X. D.; Li, J.; Ren, X. B.; Sun, J.; Ma, E.; Lookman, T. *Phys. Rev. B: Condens. Matter Mater. Phys.* **2010**, *81*, 245433.

DOI: 10.1021/acs.nanolett.7b01015
Nano Lett. 2017, 17, 3725−3730

Supplementary Information

Helium Nanobubbles Enhance Superelasticity and Retard Shear Localization in Small-Volume Shape Memory Alloy

Wei-Zhong Han[1*], Jian Zhang[2], Ming-Shuai Ding[1], Lan Lv[1], Wen-Hong Wang[3], Guang-Heng Wu[3], Zhi-Wei Shan[1*], Ju Li[1,4*]

[1]Center for Advancing Materials Performance from the Nanoscale & Hysitron Applied Research Center in China, State Key Laboratory for Mechanical Behavior of Materials, Xi'an Jiaotong University, Xi'an 710049, P.R. China

[2]College of Energy, Xiamen University, Xiamen 361005, PR China

[3]Beijing National Laboratory for Condensed Matter Physics, Institute of Physics, Chinese Academy of Sciences, Beijing, 100190, PR China

[4]Department of Nuclear Science and Engineering and Department of Materials Science and Engineering, Massachusetts Institute of Technology, Cambridge, Massachusetts 02139, USA

*Corresponding authors: wzhanxjtu@mail.xjtu.edu.cn
zwshan@mail.xjtu.edu.cn
liju@mit.edu

Figures S1-S3
Movies S1

Figure S1

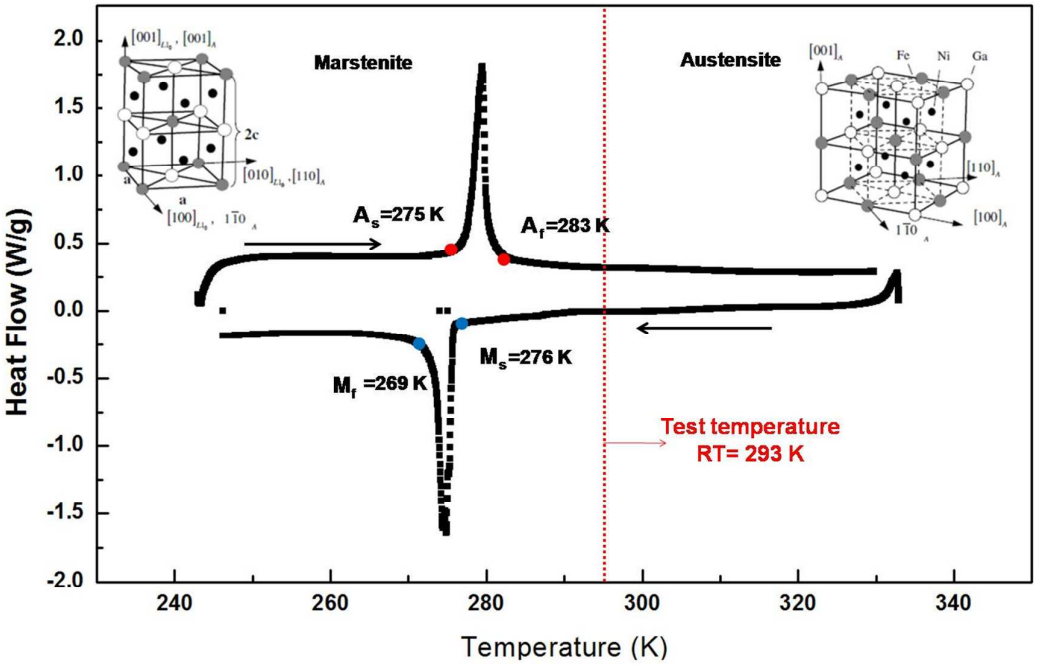

Figure S1. The typical heat flow versus temperature curves of bulk Ni-Fe-Ga shape memory alloy showing the characteristic phase transformation temperature.

Figure S2

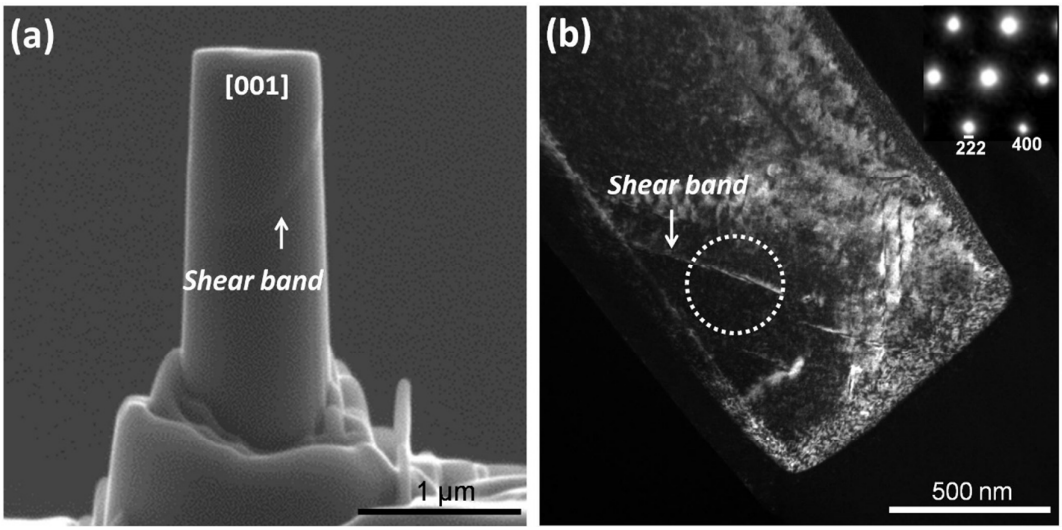

Figure S2. (a) A [001] Ni-Fe-Ga pillar with diameter of ~800 nm was loaded to form a major shear band; (b) TEM image of thin foils cutting from (a) shows the plastic deformation in original austenite phase other than the formation of stabilized martensites. The selected area diffraction was performed across the pillar and only diffraction pattern of austenite phase was obtained.

Figure S3

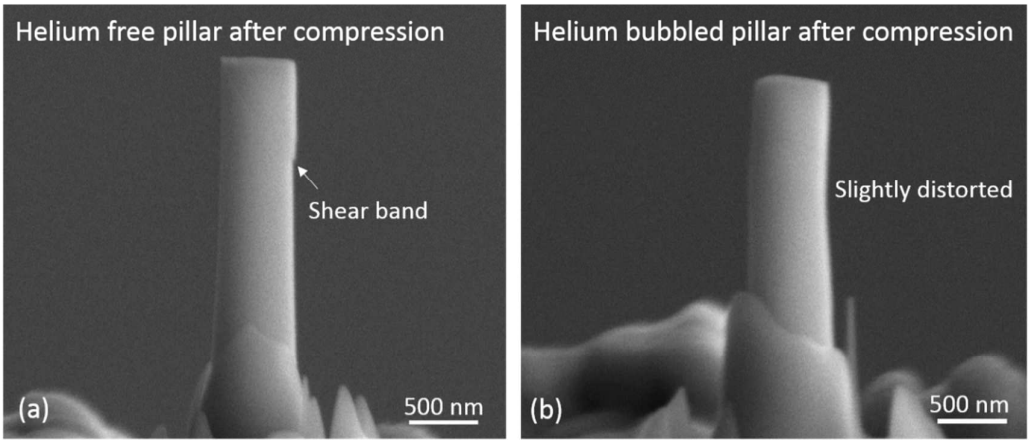

Figure S3. Typical SEM image of Ni-Fe-Ga pillars with diameter of 500 nm after compression: (a) Shear band forms on helium free pillar after loading; (b) No shear localization appears on helium bubbled pillar after loading.